Research Article

Journal of Environmental Nanotechnology

Green-synthesized WO_3–Polypyrrole Nanocomposite with Enhanced Hydrogen Sensing, Electrochemical, Photocatalytic and Antibacterial Performance

Manish Dakhore[1], Bharathi[2*], M. Kavitha[3], S. Mayakannan[4], Sudha Dukkipati[5] and S. Kannan[6]

[1]Department of Mechanical Engineering, Yeshwantrao Chavan College of Engineering, Nagpur, MH, India
[2]Department of Information Technology, M.Kumarasamy College of Engineering, Karur, TN, India
[3]Department of Mathematics, Panimalar Engineering College, Poonamallee, Chennai, TN, India
[4]School of Engineering and Emerging Technology, Rathinam Global (Deemed to be University), Coimbatore, TN, India
[4]Department of Mechanical Engineering, Saveetha School of Engineering, Saveetha Institute of Medical and Technical Sciences, SIMATS, Chennai, TN, India
[5]Department of Electrical and Electronics Engineering, Koneru Lakshmaiah Education Foundation, Vaddeswaram Guntur, AP, India
[6]Centre for Research and Innovation, Academy of Maritime Education and Training (AMET) Deemed to be University, Kanathur, Chennai, TN, India

Received: 04.09.2026 Accepted: 11.10.2026 Published: xx.xx.xxxx

*bharathiresearch4@gmail.com

ABSTRACT

This study reports a multifunctional WO_3–polypyrrole nanocomposite developed using WO_3 nanoparticles prepared from sodium tungstate dihydrate and pomegranate-peel extract. Thermogravimetric analysis, X-ray diffraction, Fourier-transform infrared spectroscopy, particle-size analysis, and scanning electron microscopy–energy-dispersive X-ray analysis confirmed the crystalline structure, interfacial interactions, thermal behaviour, elemental composition, particle distribution, and surface characteristics of the nanocomposite. The nanocomposite produced an 87.5% hydrogen response at 60 ppm and retained 88.8% of its initial response after 60 days. Electrochemical measurements conducted in three-electrode system containing 2 M KOH yielded maximum specific capacitance of 326.4 F g^{-1}, demonstrating favourable charge-storage behaviour. Under visible-light irradiation, the material degraded 96.0% of Methylene blue within 150 min. Chick embryo assessment indicated low developmental toxicity at 20 µg egg^{-1}, although adverse effects increase at higher doses. The nanocomposite also produced concentration-dependent inhibition against tested Gram-positive and Gram-negative bacterial strains, supporting its potential for antimicrobial applications.

Keywords: Green synthesis; Particle distribution; Methylene blue; Thermal behaviour; Energy storage.

1. INTRODUCTION

Inorganic–organic hybrid materials have attracted considerable research interest because combining dissimilar components can generate complementary structural, electrical, surface, and biological characteristics (Vadivel *et al.* 2025). PPy–WO_3-based nanocomposites exhibit enhanced charge transport, interfacial activity, and surface reactivity, making them suitable for photocatalysis, sensing, adsorption, and energy applications(Kashyap *et al.* 2026). Their synergistic interaction improves charge separation and overall multifunctional performance. DBSA-doped PPy–WO_3 nanocomposites by integrating tungsten oxide nanoparticles with polypyrrole in the presence of dodecylbenzene sulfonic acid as the dopant (Iyer *et al.* 2023). WO_3, boron-doped WO_3, PPy/WO_3, and PPy/WO_3–B composites through co-precipitation and polymer integration. Structural and optical characterization confirmed effective PPy coupling and boron-induced modification of WO_3, leading to reduced electron–hole recombination. The modified composites consequently exhibited enhanced photocatalytic degradation of methylene blue (Koysuren and Koysuren, 2023). PPy/WO_3/MWCNT ternary nanocomposites by integrating WO_3 nanoparticles with polypyrrole and multiwalled carbon nanotubes. Morphological and interfacial characterization indicated improved conductive pathways, charge transfer, and active-site accessibility. The optimized composite produced 98.2% dye degradation together with efficient HER and OER activity (Ahmad *et al.* 2026).

Ag-modified ZnO/cellulose acetate/PPy nanofibers containing 0.05 wt.% ZnO through electrospinning. The SEM and TEM studies revealed uniform nanofibers with diameters of 125–170 nm, while XRD and FTIR confirmed hybrid formation and Ag incorporation. The nanofibrous composite achieved 93.5% malachite-green degradation within 1 h (Elkady and Hassan, 2021), (Jachak *et al.* 2026). PPy–SnO_2, PPy–TiO_2, and PPy–TiO_2–SnO_2 nanocomposites for CO_2

sensing and characterized their structural and electrical behaviour. The heterointerfaces facilitated carrier modulation during gas adsorption. CO_2 sensitivities of 3.43, 14.15, and 8.09 were obtained, with the ternary composite showing 184 s response and 76 s recovery times (Tiwari *et al.* 2026). An EcTI-functionalized PPy/MWCNT/TiO_2 nanostructured biosensor and characterized its surface architecture using AFM. The analysis confirmed successful biomolecule immobilization and nanoscale surface modification. Detection limits of 0.56 ng mL^{-1} for PSA and 0.46 cells mL^{-1} for PC-3 cells were achieved (de Santana *et al.* 2026).

A rod-shaped WO_3/PPy photocathode containing traces of WS_3 and evaluated its structural and optical properties. Characterization indicated a crystallite size of 71 nm and an optical band gap of 2.26 eV. The photocathode generated approximately 30 µmol H_2 per 10 cm^2 h^{-1} (Rabia and Alnuwaiser, 2025). PPy/$ZnFe_2O_4$–WO_3 nanocomposites through UV-assisted photolysis for catalytic biodiesel production. Structural and surface characterization indicated enhanced reactant diffusion and improved catalytic interfacial activity. The optimized catalyst achieved a maximum biodiesel yield of 94% (Hsu *et al.* 2025). PPHC@TiO_2/PPy using pomegranate-peel hydrochar, TiO_2 nanoparticles, and polypyrrole. Structural and surface characterization confirmed a mesoporous architecture with strong interfacial interaction toward Congo Red molecules. The composite exhibited a maximum adsorption capacity of 356.61 mg g^{-1} (Alorabi, 2025).

PPy/pomegranate-peel-powder composites through oxidative polymerization using 15–20 µm peel particles. Structural and thermal characterization demonstrated modification of the PPy matrix following biomass incorporation. More than 83% of the Ni(II) adsorption capacity was attained within 60 min (Pashaei and Hosseinzadeh, 2023). PDA@PPy nanocomposites into quaternary ammonium chitosan/aldehyde dextran hydrogels through Schiff-base crosslinking. The resulting porous conductive network combined PPy-derived electrical activity with antibacterial and bioactive functionality (Nie *et al.* 2026). porous PHA monoliths composed of PHB and P4HB-containing copolymer with polypyrrole using oxidative chemical vapor deposition. The PPy layer provided conductivity and bioactivity while the PHA framework maintained mechanical stability and moisture absorption (Kovalcik *et al.* 2026).

The novelty of this study lies in the green synthesis and multifunctional integration of a WO_3–polypyrrole nanocomposite, combining hydrogen sensing, supercapacitor charge storage, visible-light photocatalytic degradation, antimicrobial activity, and chick-embryo biosafety assessment within a single material platform. The use of pomegranate-peel extract for WO_3 nanoparticle synthesis further introduces an environmentally sustainable route while maintaining strong functional performance across diverse applications.

2. MATERIALS AND METHODS

Sodium tungstate dihydrate, pyrrole, ammonium persulfate, potassium hydroxide, hydrochloric acid, ethanol, and Methylene blue were obtained in analytical grade from Sigma-Aldrich and used without further treatment (Ashrafi-Saiedlou *et al.* 2025). Fresh pomegranate peels were collected locally, thoroughly washed, shade-dried, and processed for extract preparation. Distilled water was employed throughout the synthesis and analytical procedures. Fertilized chicken eggs required for the chick embryo model were obtained from a certified local hatchery and screened for shell damage before incubation.

2.1 Pomegranate-peel-assisted Preparation of WO_3 Nanoparticles

Pomegranate peels were washed, shade-dried, and pulverized. The powder (8 g) was extracted in 120 mL of deionized water at 65 °C for 60 min. After cooling, the liquid was filtered and stored at 5 °C. Sodium tungstate dihydrate solution (120 mL, 0.08 M) was stirred for 25 min before adding 25 mL of the prepared extract.

The suspension was adjusted to pH 1.8 ± 0.1 using 0.8 M HCl and maintained at 75 °C under continuous stirring for 150 min. The resulting yellow precipitate was aged for 18 h, recovered by centrifugation at 7500 rpm for 12 min, washed four times and dried at 90 °C for 10 h. The dried precursor was calcined at 525 °C for 3 h using heating rate of 4 °C min^{-1} to obtain WO_3 nanoparticles.

Principal reactions are represented as follows:

(i) Acidification of tungstate ions:

$$Na_2WO_4 \cdot 2H_2O + 2HCl \rightarrow H_2WO_4 + 2NaCl + 2H_2O$$

(ii) Thermal conversion of tungstic acid:

$$H_2WO_4 \rightarrow WO_3 + H_2O$$

Phytochemicals present in the pomegranate-peel extract assisted nucleation, controlled particle growth, and limited excessive aggregation during WO_3 formation.

2.2 Preparation of Polypyrrole

Polypyrrole was produced through low-temperature oxidative polymerization. A 0.12 M pyrrole solution was prepared in 80 mL of 0.40 M HCl and stirred at 3 ± 1 °C for 20 min. Ammonium persulfate solution (0.15 M) was introduced dropwise over 40 min while

Article in Press

maintaining a pyrrole-to-oxidant molar ratio of 1:1.25. Polymerization was continued for 5 hours under constant stirring, after which the black suspension was kept undisturbed for 16 hours. The precipitate was filtered and repeatedly washed by deionized water and ethanol to remove residual oxidant, acid, and unreacted monomer. The purified product were dried at 55 °C for 18 hours and ground into a uniform powder.

The simplified polymerization stages are:

(i) Formation of pyrrole radical cations:

$C_4H_5N + S_2O_8^{2-} \rightarrow C_4H_5N^{\bullet+} + 2SO_4^{2-}$

(ii) Radical coupling and chain propagation:

$nC_4H_5N^{\bullet+} \rightarrow (C_4H_3N)_n + 2nH^+$

2.3 Formation of the WO_3–polypyrrole Nanocomposite

WO_3 nanoparticles (0.75 g, corresponding to a nominal loading of 15 wt.%) were dispersed in the acidified pyrrole solution by ultrasonication for 40 min. The dispersion was subsequently stirred for 35 min at 3 ± 1 °C. Ammonium persulfate was then added slowly, and polymerization was allowed to proceed for 5 hours. During polymer growth, WO_3 particles became incorporated within the developing polypyrrole network. The resulting black composite was separated by filtration, washed five times using deionized water, ethanol, dried at 55 °C for 20 hours. The dry material was gently pulverized and stored in an airtight container before characterization.

2.4 Electrochemical Measurements

Nickel foam pieces measuring 1.2 × 1.0 cm² were cleaned successively with dilute HCl, ethanol, and deionized water before electrode preparation. The working-electrode mixture contained 82 wt.% WO_3–polypyrrole, 10 wt.% conductive carbon, and 8 wt.% polyvinylidene fluoride binder. Approximately, 2.4 mg of active material was uniformly deposited on each nickel-foam collector (Zheng *et al.* 2025).

Electrochemical testing was performed in three-electrode cell containing 2 M KOH. The coated nickel foam, Ag/AgCl, and platinum foil served as working, reference, and counter electrodes, respectively. Cyclic voltammetry was conducted in the potential window −0.05 to 0.75 V at scan rates of 5, 10, 20, 40, 60, and 80 mV s^{-1}. Galvanostatic charge–discharge measurements were obtained at 0.5, 1, 2, 3, 4, and 6 A g^{-1}. Electrochemical impedance spectroscopy was performed from 0.05 Hz to 200 kHz by 10 mV alternating signal.

Specific capacitance from cyclic voltammetry was calculated by:

$$C_{sp} = \int I\, dV / (m \times \nu \times \Delta V) \quad \ldots (1)$$

Specific capacitance from the curve was determined from:

$$C_{sp} = I \times \Delta t / (m \times \Delta V) \quad \ldots (2).$$

where I represents current, m is active-material mass, ν denotes scan rate, Δt is discharge time, and ΔV is the effective potential interval. Power and energy densities were obtained using:

$$E = C_{sp} \times (\Delta V)^2 / 7.2 \quad \ldots (3)$$

$$P = 3600 \times E / \Delta t \quad \ldots (4),$$

where E and P are expressed as Wh kg^{-1} and W kg^{-1}, respectively.

2.5 Fabrication of the Hydrogen-sensing Electrode

Printed-circuit boards were employed as gas-sensor substrates. After cleaning the conductive surface, a sensing region of 0.8 cm² was defined using a positive resist. Unprotected copper was removed with ferric chloride, and the remaining resist was dissolved using acetone. A stable suspension of the WO_3–polypyrrole nanocomposite was deposited on the defined region by spin coating at 3500 rpm for 4 min. The coated substrates was dried in vacuum oven at 85 °C for 45 min to improve film adhesion and remove residual solvent. Electrical leads were attached to the contact terminals for resistance measurements. Sensor performance was examined at 35 ± 2 °C and 45 ± 3% relative humidity using hydrogen concentrations between 10 and 100 ppm.

2.6 Antibacterial Activity

Antibacterial performance of the WO_3–polypyrrole nanocomposite was examined against Gram-positive *Staphylococcus aureus* and Gram-negative *Enterobacter cloacae* and *Pseudomonas fluorescens*. Sterile Mueller–Hinton agar plates were uniformly inoculated by freshly prepared bacterial suspensions adjusted to approximately 1.5×10^8 CFU mL^{-1}. Wells of 6 mm diameter were prepared aseptically and loaded with 20, 40, 60, or 80 µL of the nanocomposite suspension. After incubation at 37 °C for 1 day, the inhibition-zone diameter surrounding each well was measured in millimetres. Three independent measurements were obtained for every treatment, and the results were expressed as mean ± standard deviation.

2.7 Photocatalytic Degradation of MB

The visible-light photocatalytic performance of WO_3–polypyrrole nanocomposite was determined using Methylene blue as the model contaminant. An 80 mg quantity of the photocatalyst were dispersed at 150 mL of

Article in Press

a 12 mg L^{-1} Methylene blue solution maintained at pH 7.2. The mixture was continuously stirred in darkness for 25 min to establish adsorption–desorption equilibrium. It was subsequently exposed to an 85 mW cm^{-2} visible-light LED source.

Aliquots of 3 mL were collected every 25 min during the 150 min irradiation period. Each sample was centrifuged to remove suspended catalyst particles, and the residual dye concentration were measured at 664 nm using UV–visible spectrophotometer. A dye solution without photocatalyst was analysed under identical conditions as a photolysis control.

Degradation efficiency (%) = $[(C_0 - C_t) / C_0] \times 100$…(5),

where C_0 represents the Methylene blue concentration after dark equilibration and C_t is its concentration after irradiation time t.

2.8 Chick Embryo Incubation and Nanocomposite Administration

Fertilized chicken eggs of comparable mass and without visible shell damage were obtained from a certified hatchery. The eggs were cleaned externally, numbered, and incubated at 37.8 ± 0.3 °C and 58 ± 4%. Automatic turning was performed regularly during the initial incubation period. Egg viability and embryo location were verified through candling before treatment.

On embryonic day 4, the eggs were randomly allocated to control and treatment groups containing 18 eggs each. The WO_3–polypyrrole nanocomposite was dispersed in sterile physiological saline and ultrasonicated to obtain a uniform suspension. Doses of 0, 20, 40, 80, or 160 µg egg^{-1} were administered through the air sac in a constant volume of 75 µL. The opening was immediately sealed using sterile paraffin film, and the eggs were returned to the incubator. Three independent experimental batches were maintained under identical conditions.

2.9 Chick Embryo Developmental-toxicity Assessment

Embryo development was evaluated on incubation days 6, 9, 12, and 15. Viability was initially determined by candling based on vascular development, movement, and heartbeat. Eggs identified as nonviable were carefully opened to confirm embryonic mortality. Surviving embryos were examined for growth restriction, haemorrhage, abnormal limb development, craniofacial defects, spinal curvature, and changes in extraembryonic blood vessels.

Survival, mortality, and malformation percentages were calculated separately for each exposure group. On day 15, the surviving embryos were removed and weighed to determine whether treatment affected developmental growth. Representative control and treated embryos were photographed under consistent magnification. All measurements were performed without knowledge of the treatment identity wherever practical, and the results were reported as mean ± standard deviation from three experimental batches.

3. RESULTS AND DISCUSSION

3.1 UV–visible Absorption and Optical Band Gap

Fig. 1 presents the UV–visible spectra and corresponding Tauc plots of WO_3, polypyrrole, and WO_3–polypyrrole. Pomegranate-peel-mediated WO_3 displayed an absorption edge near 468 nm, whereas polypyrrole produced a broad absorption band centred around 462 nm because of electronic transitions within its conjugated backbone. After composite formation, the absorption edge shifted to approximately 536 nm and extended further into the visible region. In an earlier investigation, Ni-doped PPy/TiO_2 nanocomposites using battery-recovered Ni, sugarcane-husk-derived TiO_2, and polypyrrole. UV–Vis spectroscopy revealed enhanced visible-light absorption with a narrowed optical band gap of 2.12 eV, indicating improved photoresponse. The optimized nanocomposite achieved 99.5% degradation of Rose Bengal within 4 min under sunlight irradiation (Bharti *et al.* 2026).

The estimated band gaps were 2.57 eV for WO_3, 1.66 eV for polypyrrole, and 2.31 eV for WO_3–polypyrrole. The lower value for the composite compared with WO_3 indicates modification of the interfacial electronic structure. Interaction between WO_3 and the conjugated polymer may improve visible-light harvesting and facilitate charge movement across the hybrid interface.

$$(\alpha h\nu)^2 = A\,(h\nu - E_g) \quad \ldots (6)$$

Article in Press

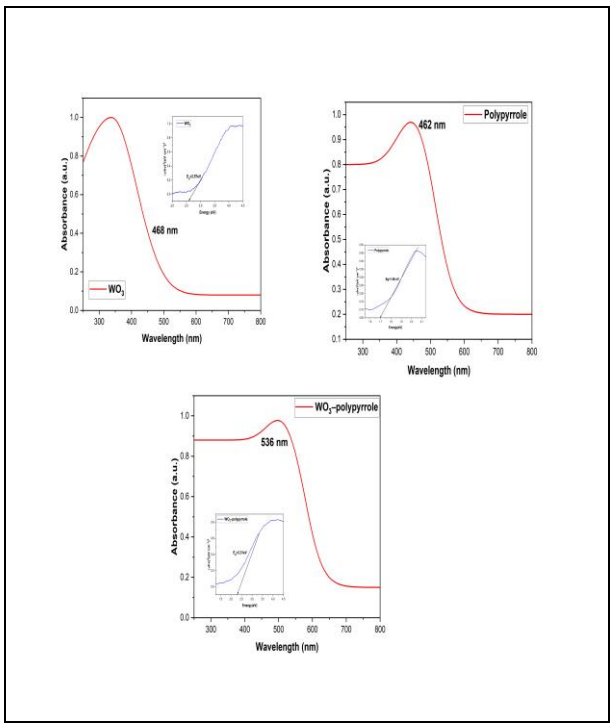


Fig. 1: UV–visible absorption spectra and Tauc of WO_3, polypyrrole, WO_3–polypyrrole nanocomposite

3.2 Fourier Transform Infrared Spectroscopy

The FTIR spectra shown in Fig. 2 verify the characteristic vibrations of WO_3 and polypyrrole within the composite. WO_3 showed peaks at 3436 and 1627 cm^{-1}, corresponding to surface hydroxyl groups and adsorbed water. Its metal–oxygen vibrations appeared at 962, 823, 736, and 587 cm^{-1} and were assigned to terminal W=O, bridging W–O–W, and O–W–O modes.

Polypyrrole exhibited peaks at 3382, 3128, 1562, 1478, 1322, 1195, and 1058 cm^{-1}. These signals were associated with N–H stretching, pyrrole-ring C=C vibration, C–N stretching, and in-plane C–H deformation. In WO_3–polypyrrole, the principal peaks occurred at 3417, 3116, 1554, 1469, 1314, 1186, 1048, 954, 814, 728, and 578 cm^{-1}. The W=O peak shifted from 962 to 954 cm^{-1}, while the W–O–W signal moved from 823 to 814 cm^{-1}. These changes support interfacial interaction between WO_3 surfaces and the polypyrrole chains. In an earlier work, WS_2@PPy nanocomposites through *in situ* oxidative polymerization, with FTIR confirming functional interaction between WS_2 and the polypyrrole matrix. The composite achieved 99% RhB degradation within 90 min under photocatalytic conditions. After five reuse cycles, the degradation efficiency remained at 96%, indicating strong structural stability (Pannerselvam *et al.* 2025).

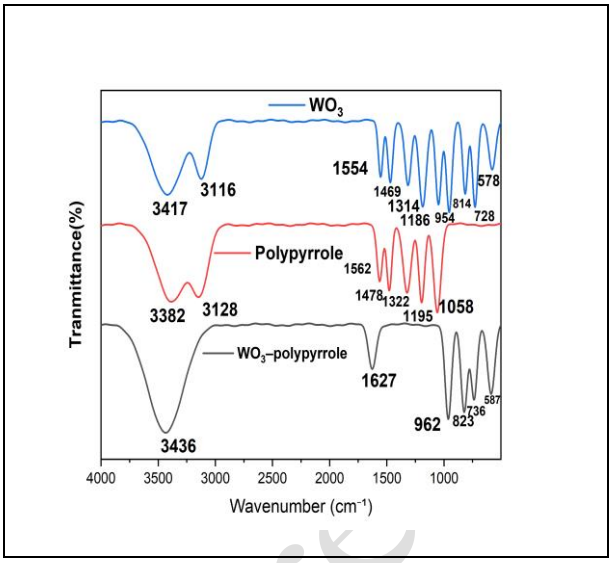


Fig. 2: FTIR spectra of WO_3, polypyrrole, and the WO_3–polypyrrole nanocomposite

3.3 Structural Analysis

Fig. 3 compares the XRD patterns of WO_3, polypyrrole, and WO_3–polypyrrole. The WO_3 pattern contained reflections at 2θ values of 22.8°, 23.5°, 24.3°, 26.5°, 28.8°, 33.1°, 34.0°, 41.5°, 49.7°, and 55.8°. These reflections were indexed to the (002), (020), (200), (120), (112), (022), (202), (222), (140), and (240) planes, confirming the formation of monoclinic WO_3.

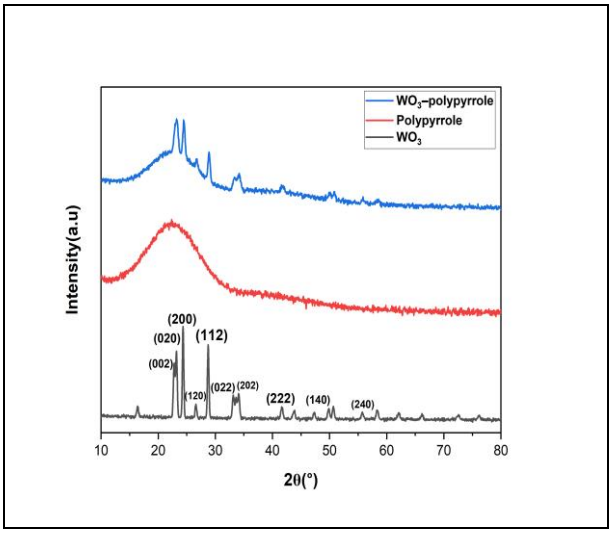


Fig. 3: XRD patterns of WO_3, polypyrrole, and the WO_3–polypyrrole nanocomposite

Polypyrrole displayed a broad maximum near 22.3°, indicating its predominantly amorphous character. The composite retained the principal WO_3 reflections, although their intensity decreased and their width increased because of polymer coverage and interfacial disorder. The average crystallite size decreased from 29.4 nm for WO_3 to 24.8 nm for WO_3–polypyrrole. The

corresponding lattice strain increased from 0.0036 to 0.0044, supporting structural modification after incorporation into the polymer network. In an earlier investigation, phytic-acid-crosslinked PANI/PPy xerogels at 1:1, 1:2, and 2:1 weight ratios through oxidative polymerization. Structural analysis by XRD confirmed successful PANI–PPy integration, while the 2:1 composition exhibited the most favorable hybrid characteristics. The optimized PANI/PPy-2:1 xerogel achieved degradation efficiencies of 91% for MB, 88% for RhB, 96% for ARS, and 92% for MO (Mir *et al.* 2024).

3.4 Surface Morphology and Elemental Composition

The surface morphology of the nanocomposite is compared with that of pure WO_3 and polypyrrole in Fig. 4(a–c). The surface of the WO_3 sample shown in Fig. 4(a) was relatively compact, irregular, and composed of plate-/flake-like domains with a few domains being smaller in size and spread over the surface. Observed morphology suggests that, the primary WO_3 particles aggregate together to form larger micron sized units during drying.

The morphology of polypyrrole in Fig. 4(b) was remarkably rough, layered and irregular comprising comparatively large agglomerated flakes. The surface is folded and fractured, typical of polymer aggregation, and creates many edges and interfaces on the surface.

The WO_3–polypyrrole nanocomposite in Fig. 4(c) exhibited a relatively rougher and more interconnected and heterogeneous morphology than the individual components. Irregular-shaped WO3-rich domains seemed to be trapped or attached to the polypyrrole matrix and small broken domains were spread around the bigger agglomerates. The intimate contact between the inorganic and polymer phases helps successfully form the composite of WO_3–polypyrrole and also creates heterogeneous interfacial regions which can facilitate the surface-mediated processes.

The EDX analysis of the nanocomposite WO_3–polypyrrole, as shown in Fig. 4(d), showed the presence of W, O, C, and N elements, indicating successful incorporation of WO_3 into the polypyrrole matrix. The elemental composition consisted of 69.2 wt.% W, 20.8 wt.% O, 7.1 wt.% C, and 2.9 wt.% N. The strong tungsten contribution and the presence of oxygen confirm the presence of the inorganic phase which is rich in tungsten, while the carbon and nitrogen content are related to the polypyrrole component. The relative contributions of W and O atoms in the corresponding structures were about 22.0% and 75.9%, respectively. The lack of strong signals of other elements indicates that the concentration of the precursor-derived elements that remain in the prepared WO_3–polypyrrole nanocomposite is relatively low. In an earlier work, PPy–TiO_2 EDX hybrid nanocomposites containing 25, 50, and 75 wt.% TiO_2 through oxidative polymerization and mechanical mixing. The residual masses at 497.80 °C were 64.82%, 60.82%, and 70.50% for the respective TiO_2 loadings, compared with 36.51% for pure PPy. The corresponding photocatalytic degradation efficiencies were 66%, 67%, and 53%, respectively (Dhachanamoorthi *et al.* 2024).

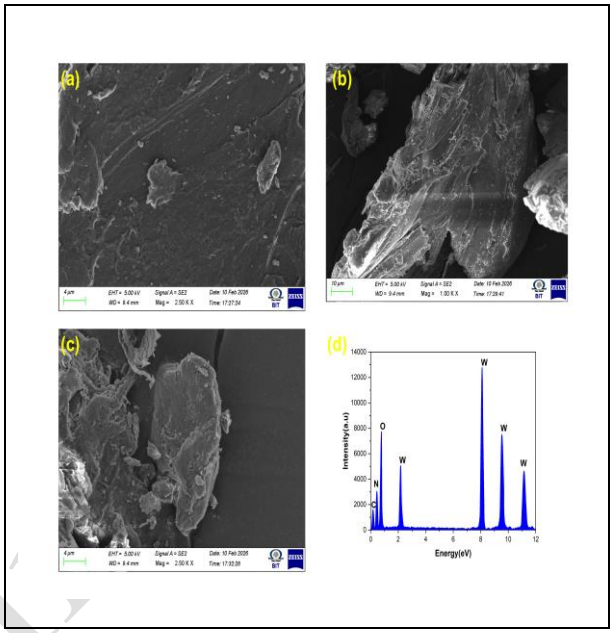


Fig. 4: SEM micrographs of (a) WO_3, (b) polypyrrole, and (c) the WO_3–polypyrrole nanocomposite and (d) EDX spectrum of the WO_3–polypyrrole nanocomposite

3.5 Thermogravimetric Behaviour

The TG, DTA, and DTG profiles of WO_3, polypyrrole, and WO_3–polypyrrole are displayed in Fig. 5–7. Measurements were performed from 30 to 850 °C under nitrogen at a heating rate of 12 °C min^{-1}. WO_3 showed mass losses of 2.5% at 30-40 °C, 2.0% at 140–330 °C, 1.8% at 330–580 °C, and 0.8% above 580 °C. The remaining mass at 850 °C was 92.9%, confirming high thermal stability. In a previous study, WO_3/TiO_2 composites modified with polyaniline, polypyrrole, and activated carbon. Thermogravimetric analysis was used to assess their thermal stability and decomposition behaviour. Among the composites, WO_3/TiO_2–AC showed the highest surface area of 127 m^2 g^{-1} and achieved 100% photocatalytic conversion (Ghoreishi *et al.* 2016).

Polypyrrole lost 6.5% below 140 °C through moisture release and 10.5% between 140 and 310 °C because of the removal of dopants and low-molecular-weight species. Decomposition of the polymer backbone caused a further 48.0% reduction between 310 and 560 °C, followed by 18.0% loss at higher temperatures. Its final residue was 17.0%.

Article in Press

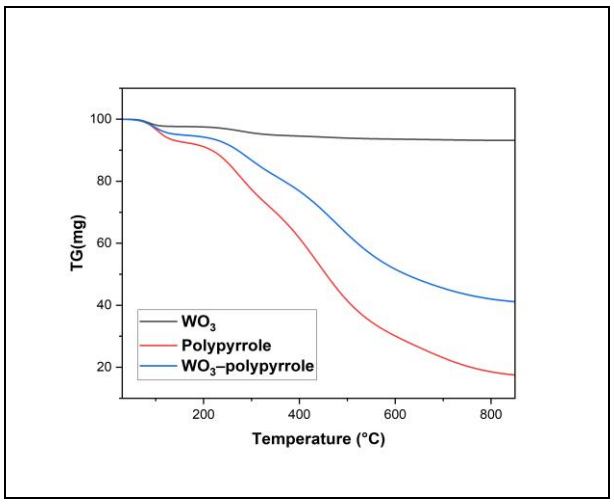


Fig. 5: TG curves of WO_3, polypyrrole, WO_3–polypyrrole nanocomposite

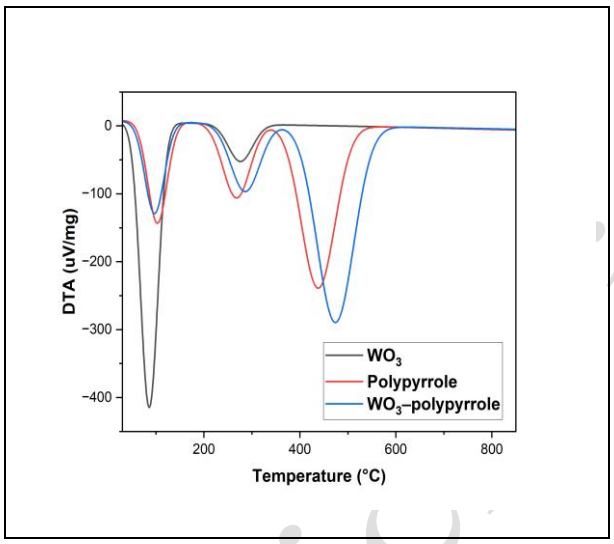


Fig. 6: DTA curves of WO_3, polypyrrole, WO_3–polypyrrole nanocomposite

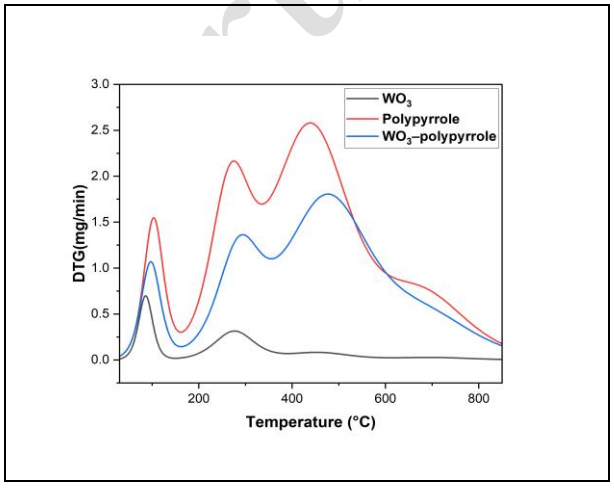


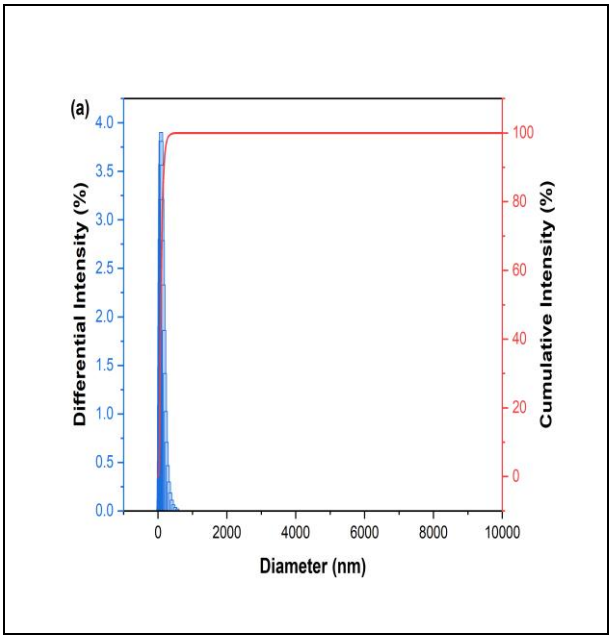
Fig. 7: DTG curves of WO_3, polypyrrole, and WO_3–polypyrrole nanocomposite

The composite exhibited losses of 5.0%, 7.5%, 30.5%, and 16.0% across the corresponding temperature intervals, leaving 41.0% residue at 850 °C. Its principal DTG occurred at 475 °C, compared with 440 °C for polypyrrole. This 35 °C shift indicates that WO_3 restricted polymer-chain decomposition and improved the thermal resistance of the hybrid structure.

3.6 Dynamic Light-scattering Analysis

Fig. 8 presents the hydrodynamic particle-size distributions. WO_3 produced average diameter of 14.6 nm polydispersity index of 0.284, whereas polypyrrole showed a larger diameter of 238.4 nm and a PDI of 0.367. The WO_3–polypyrrole nanocomposite exhibited an average hydrodynamic diameter of 176.8 nm and the lowest PDI of 0.231, indicating a comparatively narrow dispersion.

Zeta potentials of −31.4, +25.8, and −27.6 mV were obtained for WO_3, polypyrrole, and WO_3–polypyrrole, respectively. The negative value for the composite reflects the influence of surface oxygen groups contributed by WO_3. The DLS diameters exceeded the SEM measurements because the former include the surrounding solvation layer and small particle associations in suspension. In a previous work, PPy@MSN nanocomposite functionalized with methacrylate-based copolymers was developed for doxorubicin delivery. The carrier showed a drug loading capacity of 41.5%, loading efficiency of 83.1%, and particle size below 300 nm. Its pH-, GSH-, and NIR-responsive behavior supported controlled chemo-photothermal treatment (Zhang *et al.* 2026).



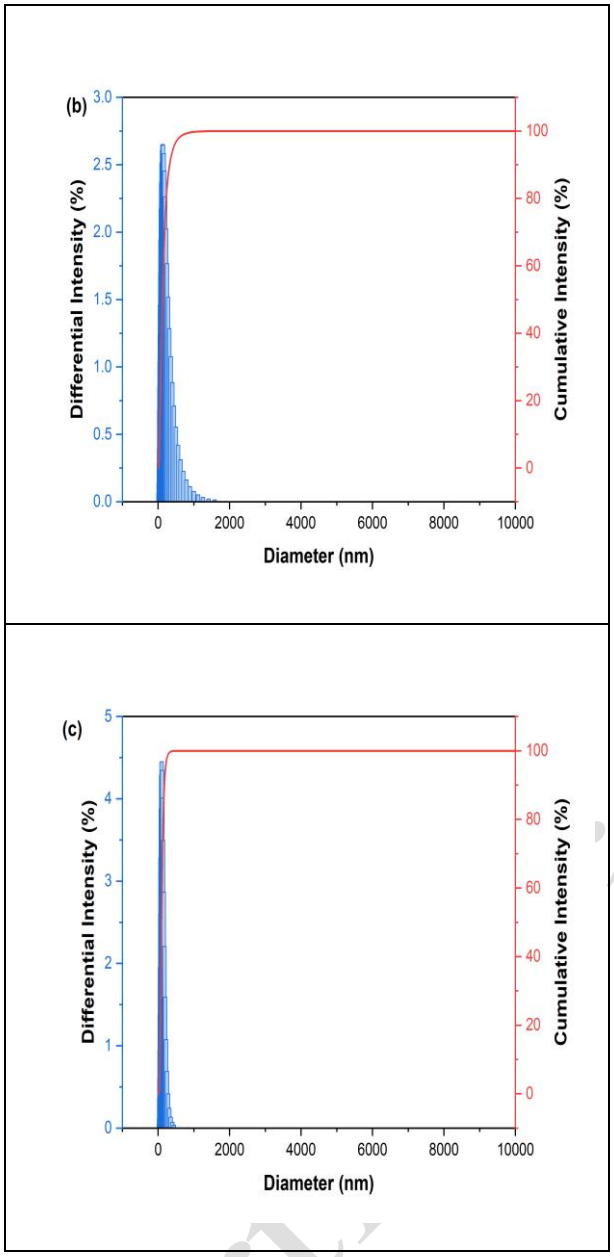


Fig. 8: DLS distributions of (a) WO_3, (b) polypyrrole, and (c) the WO_3–polypyrrole nanocomposite

3.7 Gas Sensing Performance

Selectivity was evaluated by exposing WO_3, polypyrrole, and WO_3–polypyrrole sensors to 60 ppm of H_2, NH_3, CO, CO_2, and LPG at 35 ± 2 °C and 45 ± 3% relative humidity. Each measurement was repeated three times, and the mean responses with standard deviations are presented in Fig. 9. The WO_3–polypyrrole electrode produced an H_2 response of 88.7 ± 2.3%, substantially exceeding its responses to NH_3 (32.5 ± 1.2%), LPG (26.1 ± 1.0%), CO (18.8 ± 0.8%), and CO_2 (10.4 ± 0.5%).

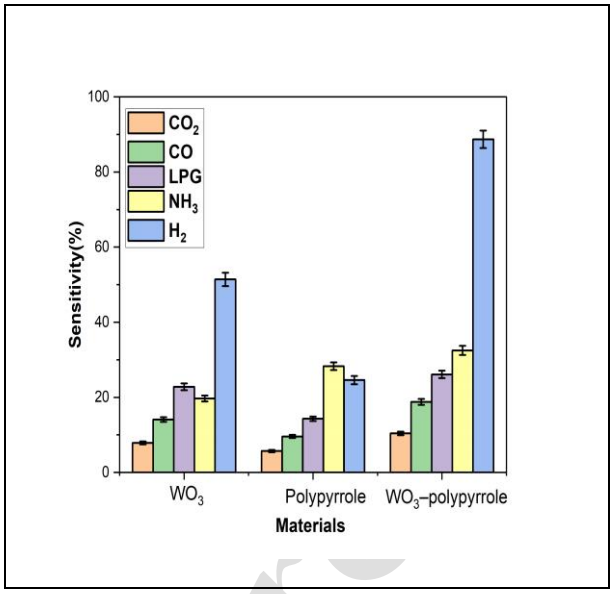


Fig. 9: Selectivity of WO_3, polypyrrole, and WO_3–polypyrrole sensors toward different gases at 60 ppm

Pure WO_3 and polypyrrole generated H_2 responses of 51.4 ± 1.8% and 24.6 ± 1.1%, respectively. The stronger behaviour of the composite is associated with the high diffusivity of hydrogen, accessible surface sites, oxygen vacancies, and charge redistribution across the WO_3–polypyrrole interface. These features produce a larger resistance change for H_2 than for the other gases examined. In an earlier work, PPy/GaN hybrid sensing films were developed by combining MOCVD-grown GaN nanostructures with *in situ* polymerized polypyrrole for room-temperature NH_3 detection. The optimized PPy/GaN-1 sensor operated over 100 ppb–1000 ppm and achieved low-concentration gas prediction with an error of 1.17 ppm using machine learning (Jia *et al.* 2026).

3.7.1 Hydrogen-response Characteristics

The electrical response was recorded using a picoammeter/voltage-source system. The percentage response was determined from the normalized resistance change:

$$S\ (\%) = |R_{air} - R_{gas}| / R_{air} \times 100 \qquad \ldots (7)$$

R_{air} is sensor resistance in air and R_{gas} is resistance after introducing test gas. The recovery and response times were defined as periods required to reach 90% of total resistance after introducing and removing hydrogen, respectively.

As shown in Fig. 10, the response of WO_3–polypyrrole increased from 28.4% at 10 ppm to 109.6 % at 100 ppm. Intermediate responses of 3.2, 65.8, 87.5, and 102.3% were measured at 20, 40, 60, and 80 ppm, respectively. At 60 ppm, WO_3–polypyrrole required 22 s to respond and 47 s to recover. These values were shorter than those of the individual materials, indicating more

efficient surface reaction and interfacial charge transfer. In an earlier research, electropolymerized PPy electrodes were developed with deposition times of 300–1800 s, producing progressively developed cauliflower-like conductive structures. The optimized 50-cycle PPy electrode delivered 412 F g^{-1}, while the symmetric device achieved 10.29 Wh kg^{-1} energy density and 146 W kg^{-1} power density at 0.1 A g^{-1} (Pham *et al.* 2026).

Table 1. Hydrogen-sensing parameters at 60 ppm

Material	Response (%)	Response Time (s)	Recovery Time (s)
WO_3	49	31	78
Polypyrrole	21.6	44	105
WO_3–polypyrrole	87.5	22	47

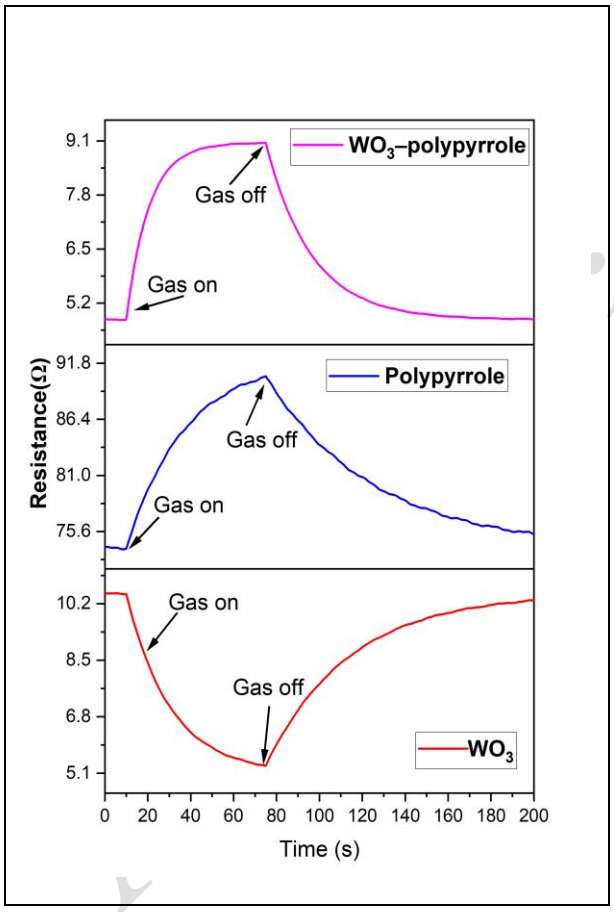


Fig. 10: Concentration-dependent hydrogen response of the WO_3–polypyrrole sensor from 10 to 100 ppm

3.7.2 Sensor Stability

Long-term repeatability was examined over 60 days using 60 ppm H_2. The initial response was assigned a retention value of 100%. Retained responses of 0 to 88.0%, 86.9%, 85.9%, 84.8%, and 83.3%were recorded after 12, 24, 36, 48, and 60 days, respectively. The limited loss of 5.5% indicates that the sensing layer preserved its electrical continuity and surface activity during storage. The WO_3–polypyrrole electrode therefore displayed acceptable stability for repeated low-temperature hydrogen detection.

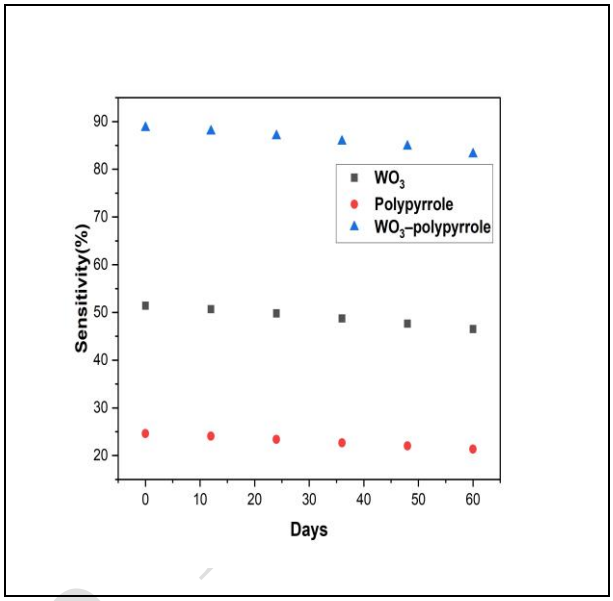


Fig. 11: Response retention of the WO_3–polypyrrole sensor toward 60 ppm H_2 over 60 days

3.7.3 Hydrogen-sensing Mechanism

When the WO_3–polypyrrole surface was exposed to air, oxygen molecules in WO_3 and capture conduction-band electrons. At the operating temperature of 35 ± 2 °C, molecular oxygen ions are expected to dominate:

$$O_2(gas) \rightarrow O_2(ads) \quad \ldots (8)$$

$$O_2(ads) + e^- \rightarrow O_2^-(ads) \quad \ldots (9)$$

Electron withdrawal generates a surface-depletion region and increases the resistance of the WO_3 component. After H_2 is introduced, it reacts with the adsorbed oxygen ions and releases the trapped electrons:

$$2H_2 + O_2^-(ads) \rightarrow 2H_2O + e^- \quad \ldots (10)$$

The returned electrons reduce the depletion width and alter the electrical resistance. Polypyrrole provides a conductive pathway and forms an interfacial junction with WO_3. Changes in carrier concentration at this junction amplify the resistance variation produced by the surface reaction. In a previous work, a PVA/PPy conductive hydrogel for room-temperature hydrogen sensing. The PPy-coated hydrogel exhibited a sensitivity of 58.468 µA M^{-1}, a detection limit of 3.435 µM, and rapid response/recovery times of 1.1/1.6 s (Seleka *et al.* 2025).

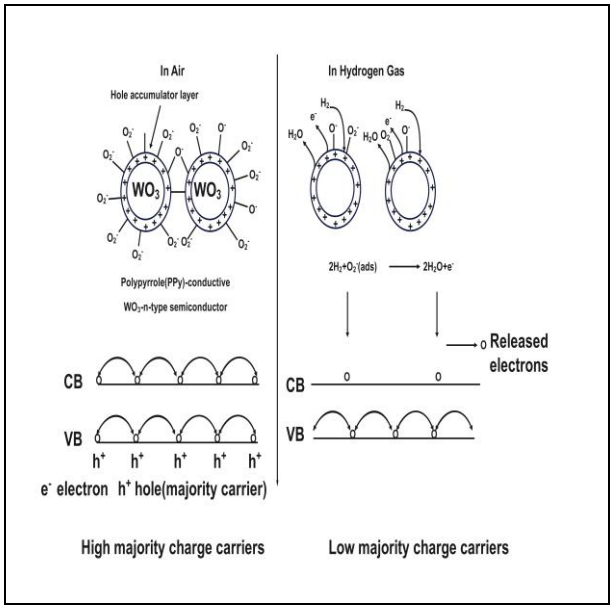


Fig. 12: Proposed hydrogen-sensing mechanism of the WO_3–polypyrrole nanocomposite: (a) oxygen adsorption in air and (b) electron release during H_2 exposure

3.8 Electrochemical Analysis

3.8.1 Cyclic Voltammetry Analysis

Charge-storage behaviour of WO_3, polypyrrole, and WO_3–polypyrrole electrodes was evaluated by cyclic voltammetry in 2 M KOH. Measurements were conducted at -0.05 and 0.75 V versus Ag/AgCl at scan rates of 5, 10, 20, 40, 60, and 80 mV s^{-1}. As shown in Fig. 13, the WO_3–polypyrrole curves retained a broad quasi-rectangular profile with weak redox contributions, indicating combined double-layer and pseudocapacitive charge storage. In an earlier research, PPy films at $scCO_2$-in-water electrolyte and evaluated electroactive behavior by cyclic voltammetry by $[Fe(CN)_6]^{3-}/[Fe(CN)_6]^{4-}$ redox probe. Increasing C/W ratio from 20/80 to 60/40 and charge density as 0.5 to 2.0 C cm^{-2} raised the relative electroactive area and accessible ion-transport pathways (Vinaisuratern *et al.* 2026).

The enclosed CV area and current response increased with scan rate without substantial distortion.

WO_3–polypyrrole delivered high specific capacitance of 326.4 F g^{-1} at 5 mV s^{-1}. The value gradually decreased to 211.8 F g^{-1} at 80 mV s^{-1} because of limited ion diffusion at increased polarization rates. At 5 mV s^{-1}, the composite capacitance exceeded those of WO_3 and polypyrrole by 84.6 and 33.4%, respectively.

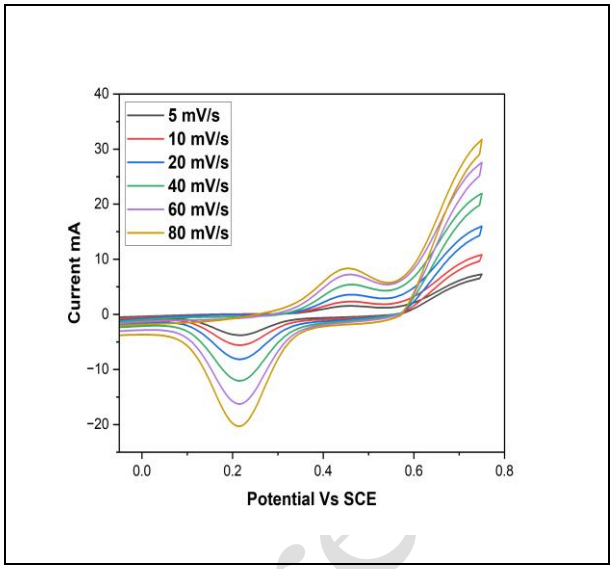


Fig. 13: Cyclic voltammograms of WO_3–polypyrrole electrode at scan rates at 2 M KOH

Table 2. Specific capacitance obtained from cyclic-voltammetry measurements

Scan Rate (mV s^{-1})	WO_3 (F g^{-1})	Polypyrrole (F g^{-1})	WO_3–polypyrrole (F g^{-1})
5	176.8	244.7	326.4
10	164.5	227.3	308.6
20	149.6	207.8	285.7
40	128.9	179.6	254.3
60	112.7	158.4	231.2
80	99.5	141.8	211.8

3.8.2 Galvanostatic Charge–discharge Analysis

The WO_3–polypyrrole electrode was further examined at current densities from 0.5 to 6 A g^{-1}. The GCD profiles in Fig. 14 showed approximately symmetric charging and discharging branches with slight curvature. This behaviour supports a reversible capacitive response involving both interfacial ion adsorption and Faradaic reactions.

The electrode delivered 312.6 F g^{-1} at 0.5 A g^{-1}. Increasing the density to 1, 2, 3, 4, and 6 A g^{-1} reduced the corresponding capacitance to 294.8, 271.5, 249.7, 231.4, and 203.6 F g^{-1}. Nevertheless, the electrode retained 65.1% of its low-current capacitance at 6 A g^{-1}, indicating useful rate capability. The gradual shortening of discharge time at higher current density arose from reduced electrolyte-ion penetration into the internal active regions. In an earlier work, flexible PPy/PVA/TiO_2/GQD nanocomposite films, where GQD incorporation markedly improved galvanostatic charge–discharge performance. Specific capacitance increased from 72.6 to 219.4 F g^{-1}, with energy density rising from

1.23 to 3.73 Wh kg^{-1} and stable operation over 5000 cycles (Salman *et al.* 2025).

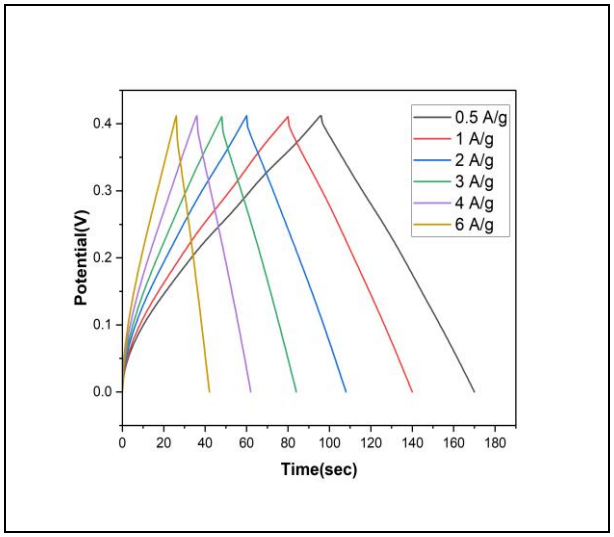


Fig. 14: Galvanostatic charge–discharge curves of the WO_3–polypyrrole electrode at different current density

3.8.3 Electrochemical-impedance Analysis

Electrode resistance and ion-transport behaviour were investigated by EIS between 0.05 Hz and 200 kHz using a 10 mV perturbation. The Nyquist plots in Fig. 15 contain a high-frequency intercept, a compressed semicircle, and an inclined low-frequency region. The intercept represents solution and contact resistance, semicircle responds to charge-transfer resistance, and low-frequency slope reflects diffusion and capacitive behaviour.

Prior to cycling, the impedance of the WO_3–polypyrrole electrode was about 40 Ohm (Z′) and 52 Ohm (Z″). The values after cycling were significantly raised to about 680 Ω (Z′) and 1280 Ω (Z″), respectively, reflecting the increase in the resistance to charge and ion transport after electrochemical cycling for long periods. In a previous work, an ultrasonically synthesized ZnO–PPy nanocomposite achieved 99.2% Cr(VI) reduction with a constant rate of 0.2572 min^{-1} under visible light. Impedance analysis confirmed improved charge-transfer behavior and reduced electron–hole recombination, while the catalyst retained high activity after four cycles (Balakumar and Baishnisha, 2021).

The favourable impedance behaviour can be attributed to the conductive polypyrrole pathways, nanoscale WO_3 redox sites, and increased interfacial contact within the composite. These components jointly support electron conduction and ionic movement, explaining the improved CV and GCD performance.

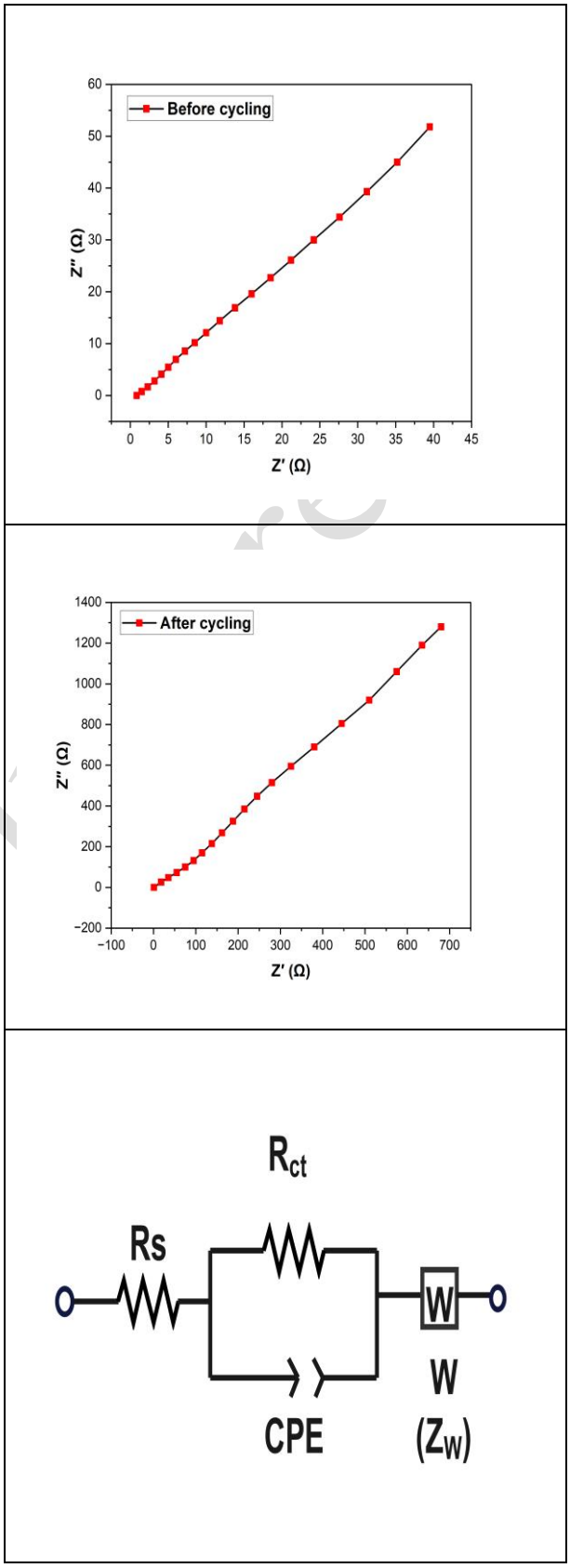


Fig. 15: Nyquist plots of WO_3, polypyrrole, and WO_3–polypyrrole electrodes with the fitted equivalent circuit

3.9 Photocatalytic Analysis

Fig. 16 presents visible-light degradation of Methylene blue by WO_3–polypyrrole nanocomposite. The initial absorption maximum at 664 nm progressively declined as irradiation proceeded, confirming removal of the dye chromophore. Degradation efficiencies of 27.0, 49.2, 66.1, 79.6, 90.0, and 96.0%were obtained after 25, 50, 75, 100, 125, and 150 min, respectively.

After 150 min, Methylene blue removal reached only 5.8% without a catalyst and 41.3% with polypyrrole. WO_3 produced 78.4% degradation, whereas WO_3–polypyrrole achieved 96.0%. The apparent pseudo-first-order rate constants were 0.0034, 0.0096, and 0.0209 min^{-1} for polypyrrole, WO_3, and WO_3–polypyrrole, respectively. The composite kinetic fit produced an R^2 value of 0.995. Its improved performance is associated with broader visible-light absorption, increased surface adsorption, and reduced charge-carrier recombination at the hybrid interface.

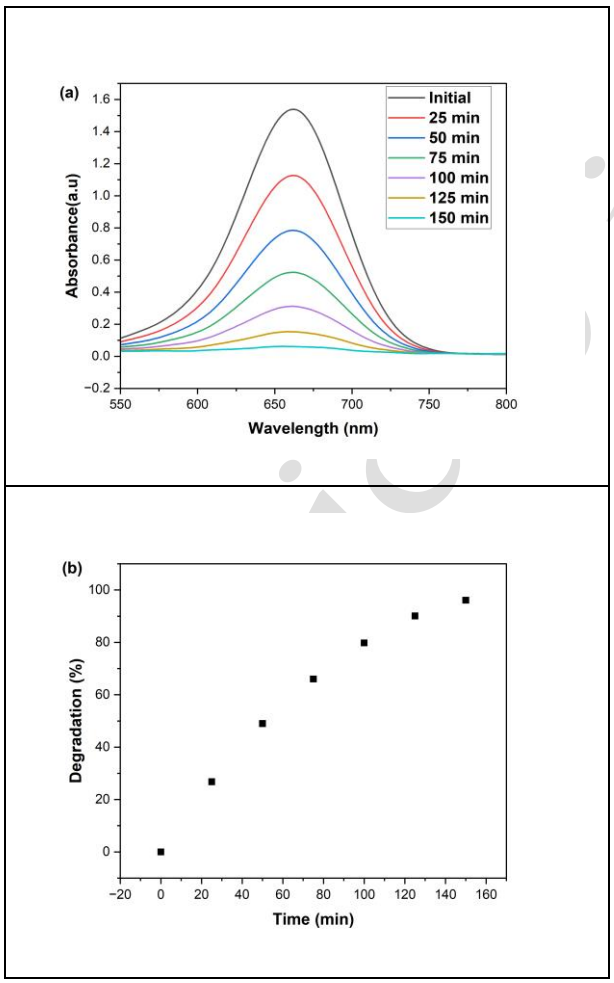


Fig. 16: Photocatalytic removal of Methylene blue using the WO_3–polypyrrole nanocomposite: (a) time-dependent UV–visible spectra and (b) degradation efficiency under visible-light irradiation

3.9.1 Photocatalytic Separation Mechanism

Visible-light absorption by WO_3 generates conduction-band electrons and valence-band holes:

$$WO_3 + h\nu \rightarrow WO_3(e^-CB + h^+VB) \quad \ldots (11)$$

The interfacial contact with polypyrrole facilitates charge transport and reduces direct electron–hole recombination. Electrons transferred through the hybrid structure react with dissolved oxygen to produce superoxide radicals:

$$O_2 + e^- \rightarrow O_2\bullet^- \quad \ldots (12)$$

Valence-band holes interact with water or hydroxide ions to generate hydroxyl radicals:

$$H_2O + h^+ \rightarrow \bullet OH + H^+ \quad \ldots (13)$$

$$OH^- + h^+ \rightarrow \bullet OH \quad \ldots (14)$$

The generated reactive species attack the aromatic structure of Methylene blue and convert it into smaller intermediates, which undergo further oxidation:

$$\text{Methylene blue} + O_2\bullet^-/\bullet OH \rightarrow \text{intermediates} \rightarrow CO_2 + H_2O \quad \ldots (15)$$

Polypyrrole contributes to visible-light absorption and provides an interfacial pathway for charge migration, while WO_3 supplies photoactive surface sites. Their combined action increases reactive-species formation and explains the higher degradation rate of the nanocomposite. In an earlier research, the optimized SnO_2/PPy nanocomposite containing 10 wt.% SnO_2 exhibited strong visible-light photocatalytic activity. The composite achieved 89% degradation of Reactive Black 31 and 98% degradation of 4-chlorophenol. Its photocatalytic rate was reported to be nearly 2 times higher than that of pristine SnO_2, indicating improved charge-transfer efficiency (Parveen *et al.* 2022).

3.10 Chick Embryo Developmental-toxicity Assessment

Fig. 17 presents the developmental response of the Chick embryo model following exposure to WO_3–polypyrrole doses of 0, 20, 40, 80, and 160 µg egg^{-1}. Embryos receiving 20 µg egg^{-1} showed 92% survival, 8% mortality, and 4% malformation on day 15, compared with 95, 5, and 2%, respectively, in the control group. These small differences indicate limited developmental disturbance at the lowest treatment level.

Increasing the dose produced a progressive reduction in survival. Day-15 survival values were 87, 77, and 56% at 40, 80, and 160 µg egg^{-1}, respectively. Mortality increased to 13, 23, and 44%, while malformation rates increases to 9, 18, and 36%. Mean

embryo mass also decreased from 12.36 ± 0.51 g in the control to 12.08 ± 0.48, 11.62 ± 0.55, 10.71 ± 0.63, and 9.28 ± 0.72 g with increasing dose.

At the higher exposure levels, the principal developmental alterations included reduced vascular development, localized haemorrhage, growth retardation, abnormal limb formation, and body-axis curvature. The observed dose dependence suggests that particle accumulation and oxidative stress may contribute to developmental injury. Accordingly, the material showed comparatively low toxicity at 20 µg egg^{-1} but clear adverse effects at 80 and 160 µg egg^{-1}.

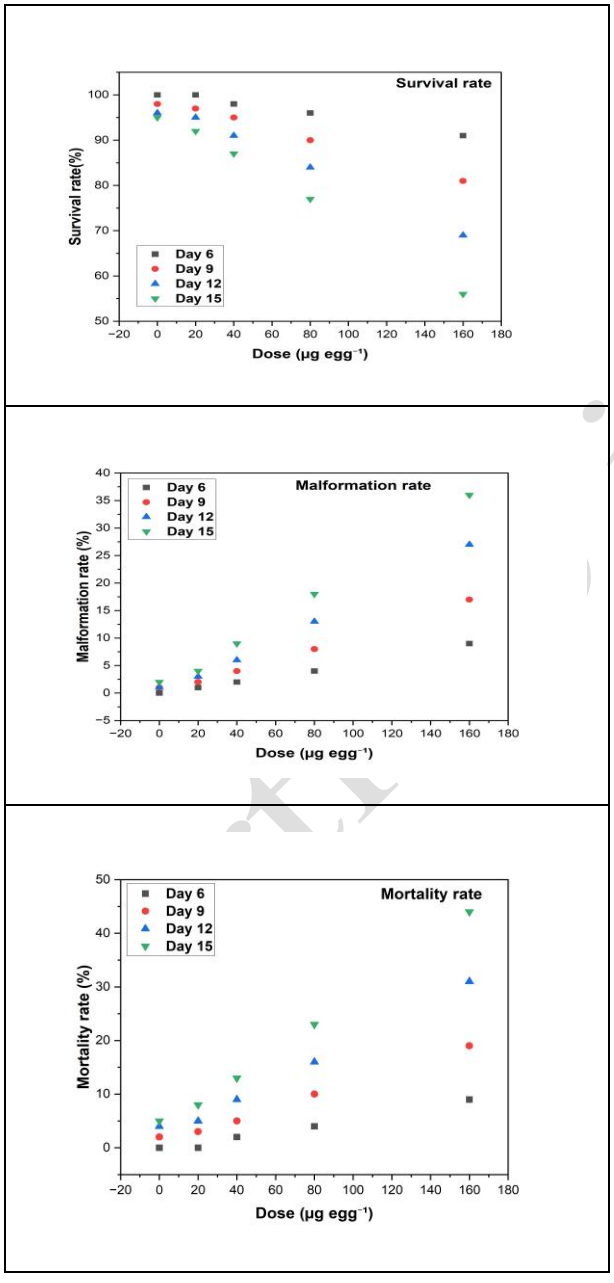


Fig. 17: Effects of WO_3–polypyrrole dose on survival, mortality, malformation, and body mass in the Chick embryo model during days 6–15

3.11 Antibacterial Activity

The WO_3–polypyrrole nanocomposite produced concentration-dependent inhibition against *Staphylococcus aureus*, *Enterobacter cloacae*, and *Pseudomonas fluorescens*, as illustrated in Fig. 18. Increasing the suspension volume from 20 to 80 µL progressively enlarged the inhibition zones for all three organisms. At 20 µL, the measured zones were 13.7 ± 0.5 mm for *S. aureus*, 12.4 ± 0.4 mm for *E. cloacae*, and 10.9 ± 0.4 mm for *P. fluorescens*. The corresponding values at 80 µL increased to 23.5 ± 0.8, 21.9 ± 0.8, and 19.7 ± 0.7 mm.

Among the examined bacteria, *S. aureus* showed the greatest susceptibility followed by *E. cloacae* and *P. fluorescens*. The MIC was 48 µg mL^{-1} for *S. aureus* and 96 µg mL^{-1} for both Gram-negative strains. The antibacterial effect may arise from contact between the nanocomposite and the bacterial envelope, followed by oxidative stress, membrane disruption, and interference with cellular processes. The lower response of the Gram-negative organisms may be associated with the additional protective barrier provided by their outer membrane. In an earlier study, Polypyrrole (Hs-PPy) and extracts of *Commiphora leptophloeos*, *Amburana cearensis*, and *Agave sisalana* against mastitis-associated *E. coli*. Hs-PPy showed bactericidal activity at 250 µg mL^{-1}, whereas *A. cearensis* required 12,500 µg mL^{-1}, indicating markedly stronger antibacterial performance of the conducting polymer (de Souza *et al.* 2026)

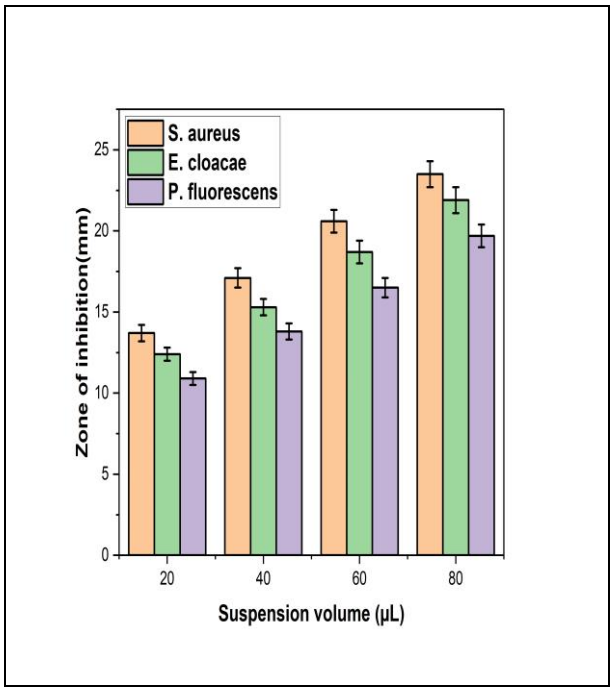


Fig. 18: Inhibition zones produced by different volumes of the WO_3–polypyrrole nanocomposite against the selected bacterial strains

Table 3. Antibacterial activity of the WO_3–polypyrrole nanocomposite

Bacterial Strain	MIC (μg mL^{-1})
S. aureus	48
E. cloacae	96
P. fluorescens	96

4. CONCLUSION

Pomegranate-peel-mediated WO_3 nanoparticles were successfully incorporated into polypyrrole to produce a multifunctional inorganic–organic nanocomposite. Structural and spectroscopic analyses confirmed monoclinic WO_3 formation and interfacial interaction with the polymer. The composite exhibited a band gap of 2.31 eV, a particle-size range of 43–91 nm, and an average particle diameter of 63.5 ± 14.8 nm. Its increased surface roughness, improved thermal resistance, and low charge-transfer resistance supported effective surface activity and carrier transport.

The WO_3–polypyrrole sensor generated an 87.5% response toward 60 ppm H_2, with response and recovery times of 22 and 47 s, respectively, while retaining 88.8% of its initial response after 60 days. The electrode reached maximum specific capacitance of 326.4 F g^{-1} at 5 mV s^{-1} and 312.6 F g^{-1} at 0.5 A g^{-1}. Under visible-light irradiation, 96.0% of Methylene blue was degraded within 150 min with a kinetic constant of 0.0209 min^{-1}. The material also produced a maximum antibacterial inhibition zone of 23.5 ± 0.8 mm against *Staphylococcus aureus*. Chick embryo assessment indicated limited developmental effects at 20 μg egg^{-1} but increasing mortality and malformation at higher doses. Overall, the nanocomposite shows potential for hydrogen sensing, electrochemical energy storage, pollutant removal, and antimicrobial applications, although further dose optimization, mechanistic investigation, and long-term safety evaluation are required.

FUNDING

This research received no specific grant from any funding agency in the public, commercial, or not-for-profit sectors.

CONFLICTS OF INTEREST

The authors declare that there is no conflict of interest.

COPYRIGHT

This article is an open-access article distributed under the terms and conditions of the Creative Commons Attribution (CC BY) license (http://creativecommons.org/licenses/by/4.0/).

REFERENCES

Ahmad, N., Kumar, G., Faridi, I. H. and Dey, R. S., Synergistic ternary polypyrrole/WO_3/MWCNT nanocomposites for environmental remediation and electrochemical water splitting, *Dalton Transac.*, 55(9), 3814–3827 (2026). https://doi.org/10.1039/d5dt02347e

Alorabi, A. Q., Sustainable Synthesis of PPHC@TiO_2/PPy Composite for Enhanced Congo Red Dye Removal: Kinetics, Isotherms, and Mechanistic Insights, *J. Clust. Sci.*, 36(5), 169 (2025). https://doi.org/10.1007/s10876-025-02898-9

Ashrafi-Saiedlou, S., Rasouli-Sadaghiani, M., Fattahi, M. and Ghosta, Y., Biosynthesis and characterization of iron oxide nanoparticles fabricated using cell-free supernatant of Pseudomonas fluorescens for antibacterial, antifungal, antioxidant, and photocatalytic applications, *Sci. Rep.*, 15(1), 1018 (2025). https://doi.org/10.1038/s41598-024-84974-0

Balakumar, V. and Baishnisha, A., Rapid visible light photocatalytic reduction of Cr^{6+} in aqueous environment using ZnO-PPy nanocomposite synthesized through ultrasonic assisted method, *Surf. Interf.*, 23, 100958 (2021). https://doi.org/10.1016/j.surfin.2021.100958

Bharti, C., Singh, A., Baghel, S. and Nandan, K., Revitalizing Battery Waste: Unveiling Ni/PPy/TiO_2-Nanocomposites for Dye Degradation, *Chem. Afr.*, 9(2), 114 (2026). https://doi.org/10.1007/s42250-026-01595-y

de Santana, C. G. F., Silva, S. H., de Cerqueira, B. M., Morais da Silva, L., Bezerra Filho, C. M., Oliva, M. L. V, Pereira, M. C., de Andrade, C. A. S., de Oliveira, M. D. L. and Avelino, K. Y. P. S., Nanostructured electrochemical biosensor modified with a plant-derived protein for serine protease detection in prostate cancer, *Anal. Biochem.*, 714, 116106 (2026). https://doi.org/10.1016/j.ab.2026.116106

de Souza, J. M. S., de Lima, G. B. V, Cassimiro, D. D. S., da Silva, S., Sousa, T. J., Rosa, D. S., Souza, R. F. S., da Silva Júnior, F. A. G., de Oliveira, H. P., Osaki, S. C., Azevedo, V. A. C., Brenig, B., Aburjaile, F. F. and da Costa, M. M., Evaluation of genomic characteristics of *Escherichia coli* associated with bovine mastitis and the potential utility of alternative antimicrobial methods, *Braz. J. Microbiol.*, 57(1), 221 (2026). https://doi.org/10.1007/s42770-026-02040-5

Dhachanamoorthi, N., Oviya, K., Sugumaran, S., Suresh, P., Parthibavarman, M., Jeshaa, D. K. and Aishwarya,

Article in Press

M., Effective move of Polypyrrole/TiO_2 hybrid nanocomposites on removal of methylene blue dye by photocatalytic activity, *Chem. Phys. Impact*, 9, 100723 (2024). https://doi.org/10.1016/j.chphi.2024.100723

Elkady, M. F. and Hassan, H. S., Photocatalytic degradation of malachite green dye from aqueous solution using environmentally compatible Ag/ZnO polymeric nanofibers, *Polym.*, 13(13). 2023 (2021). https://doi.org/10.3390/polym13132033

Ghoreishi, K. B., Asim, N., Che Ramli, Z. A., Emdadi, Z. and Yarmo, M. A., Highly efficient photocatalytic degradation of methylene blue using carbonaceous WO_3/TiO_2 composites, *J. Porous Mater.*, 23(3), 629–637 (2016). https://doi.org/10.1007/s10934-015-0117-4

Hsu, C. Y., Mahmoud, Z. H., Kamolova, N., Muzammil, K., Alsultany, F. H., Al-Abdeen, S. H. Z. and Kianfar, E., Photosynthesis of polypyyrole/$ZnFe_2O_4$-WO_3 nanocomposite for biodiesel production. *Fuel Proce. Technol.*, 271, 108193 (2025). https://doi.org/10.1016/j.fuproc.2025.108193

Iyer, N. V, Kher, J. A. and Bhame, S. D., Photocatalytic dye degradation using novel Polypyrrole-Tungsten Oxide hybrid nanocomposite system, *J. Water Environ. Nanotechnol.*, 8(4), 334–356 (2023). https://doi.org/10.22090/JWENT.2023.04.002

Jachak, S. R., Srinivasan, R., Arunkumar, S., Kumar, V. N., Manu, Y. M. and Mayakannan, S., Development of MUF-bonded Banyan Fiber Laminates Reinforced with Bio-synthesized CeO_2 Nanoparticles for Advanced Applications, *J. Environ. Nanotechnol.*, 15(2), 554–562 (2026). https://doi.org/10.13074/jent.2026.06.2622149

Jia, Z., Wang, W., Han, D., Yan, L., Guang, J., Duan, Q., Wang, Y., Cheng, Z., Wang, G., Wang, W. and Sang, S., RBFNN-Based PPy/GaN sensor array with wide dynamic range and sub-ppb detection for accurate ammonia identification in human exhaled breath, *Microsyst. Nanoeng.*, 12(1), 3 (2026). https://doi.org/10.1038/s41378-025-01119-7

Kashyap, D. N., Shalom, N., Mayakannan, S., Muthuraj, M., Thanikasalam, A. and Ahmed, A. A., Comparative Green and Wet-chemical Synthesis of ZnO Nanoparticles: Enhanced Photocatalytic and SERS Performance of Defect-rich Nanostructures, *J. Environ. Nanotechnol.*, 15(2), 162–175 (2026). https://doi.org/10.13074/jent.2026.06.2612090

Kovalcik, A., Cernekova, N., Fauzi, F., Bose, R. K., Spitalsky, Z., Kadlecova, Z., Vojtova, L., Víchová, Z., Humpolíček, P. and Bober, P., Conformal polypyrrole biointerfaces on porous PHA monoliths via oxidative chemical vapor deposition, *Colloids Surf. B: Biointerf.*, 261, 115417 (2026). https://doi.org/10.1016/j.colsurfb.2026.115417

Koysuren, H. N. and Koysuren, O., Improving UV Light Photocatalytic Activity of WO_3 by Doping with Boron and Compounding with Polypyrrole, *Biointerf. Res. Appl. Chem.*, 13(1), 86 (2023). https://doi.org/10.33263/BRIAC131.086

Mir, A., Aazam, E. S. and Riaz, U., Design of Phytic Acid Crosslinked Xerogels as Organic Photocatalysts for Visible Light-Assisted Degradation of Dyes, *Adv. Mater. Interf.*, 11(18), 2400046 (2024). https://doi.org/10.1002/admi.202400046

Nie, L., Wang, L., Wang, T., Deng, Y., Guo, W. and Ding, P., Conductive and antibacterial hydrogel bio-adhesives based on quaternized chitosan, aldehyde dextran, and polydopamine/polypyrrole nanocomposites, *Res. Chem.*, 29, 103668 (2026). https://doi.org/10.1016/j.rechem.2026.103668

Pannerselvam, M., Shameem, A., Dineshbabu, N., Murugan, A., Bavani, T. and Siva, V., A nanoscale tungsten disulfide decorated polypyrrole nanocomposites for effective photocatalytic degradation of Rhodamine B under visible light, *J. Mol. Struct.*, 1347, 143272 (2025). https://doi.org/10.1016/j.molstruc.2025.143272

Parveen, A., Surumbarkuzhali, N., Shkir, M., El Sayed Massoud, E., Manjunath, V., Ahn, C. H. and Park, S. H., Design of SnO_2 nanorods/polypyrrole nanocomposite photocatalysts for photocatalytic activity towards various organic pollutants under the visible light irradiation, *Inorg. Chem. Commun.*, 142, 109685 (2022). https://doi.org/10.1016/j.inoche.2022.109685

Pashaei, S. and Hosseinzadeh, S., Synthesis and Investigation of Polypyrrole/ Pomegranate Peel Powder Composites and Application for Removal of Heavy Metals from Water, *Appl. Chem. Today*, 18(68), 63–82 (2023). https://doi.org/10.22075/chem.2023.25588.2035

Pham, D., Gouafong, R., Irvin, J., McKinney, B., Dileonardi, J., Cox, M. and Aphale, A., Evolution of polypyrrole electrode during electropolymerization and its effect on energy storage performance. *Sci. Rep.*, 16(1), 11720 (2026). https://doi.org/10.1038/s41598-026-47559-7

Rabia, M. and Alnuwaiser, M. A., A One-Pot Approach for Synthesizing a Rod-Shaped Photocathode Composed of W(VI) Oxide/Polypyrrole for Sacrificial Agent-Free Green Hydrogen Production, *J. Electron. Mater.*, 54(7), 5356–5368 (2025). https://doi.org/10.1007/s11664-025-11966-9

Salman, M., Aslam, M., Mustafa, Z., Ahmad, M. and Shehzad, A., Flexible polypyrrole/polyvinyl alcohol/titanium dioxide/graphene quantum dots nanocomposite films for energy storage devices, *Diamond Related Mater.*, 152, 111996 (2025). https://doi.org/10.1016/j.diamond.2025.111996

Seleka, W. M., Phasha, M. M., Kganyakgo, L. K., Makwakwa, D. and Makhado, E., Preparation of a conductive hydrogel based on carrageenan, polyvinyl alcohol, and polypyrrole as a potential room temperature electrochemical hydrogen gas sensor, *Microchem. J.*, 214, 114091 (2025). https://doi.org/10.1016/j.microc.2025.114091

Article in Press

Tiwari, A. V., Deshmukh, A. P., Tiwari, S. P., Dudhe, P. S., Wanjari, S. S., Yawale, D. S. and Yawale, S. P., Interface-engineered novel PPy-TiO_2-SnO_2 ternary nanocomposite for high-sensitivity low-concentration CO_2 gas sensing, *Next Nanotechnol.*, 9, 100455 (2026). https://doi.org/10.1016/j.nxnano.2026.100455

Vadivel, M., Satishkumar, P., Saminathan, R., Hadidi, H. M., Sivasundar, V., Ganvir, V. Y., Mayakannan, S. and Jenifer, J. S., Influence of Saltwater and Distilled Water on the Mechanical Properties of Natural Fiber–reinforced Polyester Composites Enhanced with SiC Nanoparticles, *J. Environ. Nanotechnol.*, 14(3), 692–704 (2025). https://doi.org/10.13074/jent.2025.09.2531746

Vinaisuratern, P., Kurioka, T., Chen, C. Y., Chang, T. F. M. and Sone, M., Morphology and electrochemical accessibility of polypyrrole films electrodeposited in supercritical CO_2-in-water emulsified electrolytes, *J. Supercritical Fluids*, 238, 107095 (2026). https://doi.org/10.1016/j.supflu.2026.107095

Zhang, W., Huang, J., Li, Y., Yao, Y., Zhang, J. and Chen, M., Trace Ni doping-enhanced capacitive WO_3 electrode for high-energy-density asymmetric supercapacitors, *J. Electroanal. Chem.*, 1004, 119829 (2026). https://doi.org/10.1016/j.jelechem.2026.119829

Zheng, W., Chen, C., Chen, X., Cao, J., Chen, A., Shao, S. and Lian, Y., The design and optimization of energy level alignment in dual-photoelectrode solar PEC cells for efficient dye degradation at low bias, *Surf. Interf.*, 56, 105646 (2025). https://doi.org/10.1016/j.surfin.2024.105646

Article in Press